Deep topographic proteomics of a human brain tumour

Simon Davis[1,2], Connor Scott[3], Janina Oetjen[4], Philip D Charles[1,5], Benedikt M Kessler[1,2], Olaf Ansorge[3], Roman Fischer[1,2] *

[1] Target Discovery Institute, Centre for Medicines Discovery, Nuffield Department of Medicine, University of Oxford, Roosevelt Drive, Oxford, OX3 7FZ, UK

[2] Chinese Academy for Medical Sciences Oxford Institute, Nuffield Department of Medicine, University of Oxford, Roosevelt Drive, Oxford, OX3 7FZ, UK

[3] Academic Unit of Neuropathology, Nuffield Department of Clinical Neurosciences, University of Oxford, John Radcliffe Hospital, Oxford, OX3 9DU, UK

[4] Bruker Daltonics GmbH & Co. KG, Fahrenheitstraße 4, 28359 Bremen, Germany

[5] Big Data Institute, Nuffield Department of Medicine, University of Oxford, Roosevelt Drive, Oxford, OX3 7FZ, UK

* Corresponding author. E-mail: roman.fischer@ndm.ox.ac.uk. Phone: +44 1865 743639.

Abstract

Cellular protein expression profiles within tissues are key to understanding disease pathology, and their spatial organisation determines cellular function. To precisely define molecular phenotypes in the spatial context of tissue, there is a need for unbiased, quantitative technology capable of mapping the expression of many hundreds to thousands of proteins within tissue structures. Here, we present a workflow for spatially resolved, quantitative proteomics of tissue that generates maps of protein expression across a tissue slice derived from a human atypical teratoid-rhabdoid tumour (AT/RT). We employ spatially-aware statistical methods that do not require prior knowledge of tissue structure to highlight proteins and pathways with varying spatial abundance patterns. We identify novel aspects of AT/RT biology that map onto the brain-tumour interface. Overall, this work informs on methods for spatially resolved deep proteo-phenotyping of tissue heterogeneity. Advanced spatially resolved tissue proteomics will push the boundaries of understanding tissue biology and pathology at the molecular level.

Main

Tissues contain various microscopic features, cell types, and phenotypically diverse subpopulations. The location of cells within a tissue and their spatial neighbourhood is crucial for determining their identity and function[1–6]. The cellular composition of tissue has substantial effects on measured coexpression signals within the molecular profiles of bulk tissue, and changes in cellular tissue composition can contribute to different disease outcomes[7,8]. Changes in the composition of the surrounding microenvironment could also contribute as signals from the microenvironment influence cell functions[9]. For example, in tumours, complex signalling occurs between tumour and normal cells that have been co-opted to promote tumour cell function and survival[10,11]. Recent technology developments in DNA and RNA sequencing technologies now allow for the generation of near-complete genomes and transcriptomes. These advancements have furthered the understanding of many biological aspects from the level of cells through to populations in many human disease contexts[12–14]. Furthermore, the development of technologies capable of retaining the spatial context of these genomic and transcriptomic profiles have enabled the characterisation of spatial heterogeneity of these profiles within a tissue[15,16]. However, while genomic and transcriptomic alterations may act as drivers of disease, the proteins they code for regulate essentially all cellular processes[17].

A range of mass spectrometry (MS)-based techniques are available to map the distribution of proteins throughout tissues and cells. Mass spectrometry imaging (MSI) enables the determination of proteins or other molecules within a sample by rastering an ion source over a sample in a grid pattern. This approach can be untargeted, where the analytes are detected directly, such as matrix-assisted laser desorption/ionisation (MALDI)[18,19], or targeted where tissue is probed with metal-tagged antibodies with detection of the metal isotopes, such as in imaging mass cytometry[20,21]. Liquid extraction surface analysis mass spectrometry (LESA-MS) helps address the lack of depth in untargeted MSI and prior-knowledge requirement of targeted MSI by extracting analytes from tissue using a liquid microjunction[22]. In the case of proteins, these can be enzymatically digested and analysed by LC-MS to provide better depth and identification confidence[23]. However, LESA has limited resolution, typically ≥ 500 µm and cannot accurately sample the irregular structures present within tissue.

Laser capture microdissection (LCM) is well-placed to address the limitations of the spatially-resolved mass spectrometry methods described above[24]. LCM can extract regions from a tissue slice ranging from single cells to square millimetres of tissue[25,26]. We and others have previously described several methods coupling LCM to LC-MS, and the approach has been used to investigate a wide range of tissue biology[27–31]. Combining LCM-Proteomics with automated image analysis systems could be a powerful approach. Mund et al. recently developed the concept of Deep Visual Proteomics by combining high-resolution imaging, image analysis based on machine learning, and a sensitive proteomics workflow[32] classifying cells into subtypes using machine learning to automatically cut and capture cells based on their classification before proteomics analysis.

Generally, LCM-Proteomics has been used in a 'feature-driven' approach, where tissue regions are extracted based on existing knowledge such as histological features, immunostaining or gross morphology & macrostructures[24,33–36]. This feature-driven approach effectively investigates tissue heterogeneity. However, sampling in an unbiased manner, like MSI, could reveal novel insights into the spatial protein expression patterns within a tissue. For example, Piehowski et al. used LCM-proteomics to sample mouse uterine tissue in a rastered grid with a resolution of 100 µm and their custom, nanolitre-scale nanoPOTS sample preparation platform to quantify over 2,000 proteins within the tissue[37].

Here, we systematically performed spatially-resolved measurements of a human brain tumour proteome using laser capture microdissection to a depth of over 5,000 proteins. We use spatially aware statistical tests to identify proteins and pathways displaying differential spatial expression within tissue sections. This did not require prior knowledge of tissue structures, features, or pathology. Furthermore, clustering of protein expression and inferring pathway activity reveals new, spatially defined proteo-phenotypes within the otherwise homogeneous macrostructure of the analysed tumour.

Results

We characterised how the number of protein identifications varies with the tissue area collected by LCM on two LC-MS/MS systems, an Orbitrap Fusion Lumos mass spectrometer with 60-minute gradients and a TimsTOF Pro using 17-minute gradients. We collected areas

from 316 µm^2 to 1,000,000 µm^2 (Figure S1). Both systems perform similarly, with the Lumos system ranging from 282 – 3480 protein groups and the timsTOF system ranging from 127 – 3318 protein groups, comparing favourably to other LCM-proteomics work[25]. These searches were performed without match-between-runs to avoid boosting the IDs of the smaller areas using information from the larger areas. Areas above 316,000 µm^2 result in diminishing returns, likely caused by approaching the maximum number of MS/MS spectra that can be acquired within each system's fixed gradient times.

Proteomic topography of a human brain tumour

After characterising the upper and lower limits of the workflow, we sampled a 10 µm thick section of an atypical teratoid-rhabdoid tumour (AT/RT) block (~20 x 15 mm). The tissue was subdivided into 384 (24 x 16) square 'pixels' with an area of ~694,000 µm^2 (side length of 833 µm); each pixel was isolated by LCM and processed with our LCM-SP3 protocol[29] (Figure 1). Each sample was analysed on the 17-minute timsTOF Pro setup. In total, 5,321 proteins were identified, with 32 – 4,741 proteins identified per sample. This range includes empty pixels where no tissue was visible, demonstrating a low level of contamination throughout the workflow. Figure S2 shows the distribution of proteins identified and quantified per pixel and the number of pixels with quantitative values for each protein. The quantitative values for each protein in each pixel can be mapped back to their original positions within the tissue grid. Figure 2A shows proteomic maps for four example proteins, liver glycogen phosphorylase (PYGL), peripherin (PRPH), haemoglobin (HBB) and histone H4 (HIST1H4A), where each pixel is coloured by the normalised protein intensity of that protein in that sample. Glycogen phosphorylase releases glucose from glycogen for entry into glycolysis, and its expression in cancer is associated with malignant phenotypes, hypoxia resistance and cancer cell survival[38]. Peripherin is an intermediate filament protein without a clear function and is highly expressed during development and after nerve injury; its expression pattern is consistent with the tumour growth into surrounding normal brain tissue[39–41].

We then tested the 4,306 proteins quantified in at least 9 pixels for spatial variation using the Moran's *I* test for spatial autocorrelation[42]. Values of Moran's *I* lie between -1 and +1, where positive values indicate that areas close in space tend to have similar values, negative values indicate that areas close in space tend to have different values, and zero indicates data are randomly distributed in space. The pixels containing the large region of

haemorrhage and the empty pixels were excluded from this and further analyses. Of the proteins tested, 3,212 have a *q*-value ≤ 0.05. The summed and mean intensities of each pixel do not show significant spatial autocorrelation (I = 0.003 & 0.003, p = 0.313 & 0.317, respectively), showing that the sampling process worked well and is not a systemic cause of spatial variability (Figure S3).

In addition to the large field of view, we also sampled a smaller region with higher spatial resolution from an adjacent tissue section. These proteomic maps were generated from an area of variability identified in the H&E staining and above proteomic maps, where a region of solid tumour containing neoplastic cells meets a region we termed 'brain/tumour' interface, which has a mixture of normal and neoplastic cells along with a large, prominent blood vessel. This region was sampled with 96 pixels, 350 µm x 350 µm (122,500 μm^2) each and each pixel was analysed on the Orbitrap Fusion Lumos system using 60-minute gradients. In total, 3,994 proteins were quantified in at least one sample. The increased resolution proteomic maps for PYGL, PRPH, haemoglobin and histone H4 are shown in Figure 2B. Their expression is consistent with the large field-of-view data, with PYGL and PRPH showing opposite expression patterns across the margin between solid tumour and brain/tumour interface and haemoglobin co-localising with the visible blood vessels. Histone H4 shows even expression across the two annotated areas, with a region of lower expression corresponding with a visibly diffuse patch of tissue. Of the 3,050 proteins quantified in at least 9 pixels, 1,375 show evidence for significant spatial autocorrelation (Moran's I test, $q \leq 0.05$).

Spatial proteomics reveals PYGL, ASPH and CD45 as markers for tumour boundary

Three candidate proteins showing significant spatial variation were selected for follow-up immunohistochemistry (IHC) staining: glycogen phosphorylase, aspartate beta-hydroxylase (ASPH) and CD45 (PTPRC) to validate the spatially resolved protein expression data generated above. The IHC staining images closely resemble the protein intensity distributions (Figure 3A,C,E) within the proteomic maps for these three proteins. Both PYGL and ASPH show intense IHC staining in the region of solid tumour (Figure 3B,D), and CD45 shows intense staining in the region of tissue corresponding to the upper-left pixels in the proteomic map (Figure 3F).

Spatial proteomic mapping highlights molecular pathways underlying tissue heterogeneity

As Moran's *I* measures global autocorrelation, it does not indicate where the locations that drive the autocorrelation occur. To investigate which regions of the sampled tissue show similar expression, the data were clustered using hierarchical clustering and the resulting dendrogram was cut using the Dynamic Tree Cut method[43]. The generated cluster labelling of pixels can also be mapped back to their spatial location (Figure 4A). The clusters generally form contiguous regions in space, with some long-range co-clustering in smaller clusters. The margin between solid tumour and brain/tumour interface is well-represented by the border between cluster 1 (solid tumour) and cluster 3 (brain/tumour interface). In addition to the cluster map, the assigned clusters were plotted onto a uniform manifold approximation and projection (UMAP) visualisation[44] (Figure 4B). The clusters visible in the UMAP plot correspond well to the Dynamic Tree Cut method generated clusters.

This method generates spatially well-defined clusters, allowing for a feature-driven approach without prior knowledge of the histopathological details. Proteins quantified were tested for significantly differing intensities across the clusters using a one-way ANOVA test. There are 3,512 proteins with significant evidence ($q \leq 0.05$) for differential intensity between two or more clusters. Pairwise Tukey *post-hoc* tests were used to generate fold-change estimates between pairs of clusters, and these fold-changes were used as the input for gene set enrichment analysis. Functional analysis of clusters 1 & 3 indicates that proteins and processes involved in protein translation and modification, extracellular matrix organisation, energy pathways, mRNA processing, steroid synthesis, neuronal cell adhesion, and neuronal differentiation are differentially abundant between the region of solid tumour and brain/tumour interface (Figure 4C).

Applying the same clustering method to the high-resolution maps results in a cluster map that is broadly consistent with the low-resolution map (Figure 5A). There are generally contiguous clusters that represent the solid tumour (cluster 1), the brain/tumour interface (cluster 3), the margin between (clusters 2 & 5), and blood vessels (cluster 6). A volcano plot between cluster 3 and cluster 1 reflects what is generally seen in the proteomic maps, with large fold-changes in the abundance of PYGL, ASPH and PRPH (Figure 5B). Functional analysis of clusters 1 & 3 indicates that proteins involved in extracellular matrix, cell

adhesion & motility, angiogenesis, immune processes, epidermis function, and neuronal development are differentially abundant between solid tumour and brain/tumour interface (Figure 5C). These functional differences are broadly consistent between this high-resolution and lower-resolution sampling described above.

We investigated the expression of other immune cell-marker proteins because of the discovered differences above in immune processes and highly localised CD45 abundance and staining (Figure 6A). In general, their proteomic maps show localisation to the upper-left of the sampled region, consistent with the CD45 patterns. Marker proteins for neutrophils, neutrophil cytosolic factor 2 & 4 (NCF2 & NCF4), are present along with marker proteins for pro-tumour M2 macrophages, CD163 & mannose receptor C-type 1 (CD163 & MRC1)[44,45]. These proteins' peak expression locations correspond with clusters 13 and 6 for the neutrophil and macrophage markers, respectively. A functional analysis between these two clusters shows increased abundance for many proteins involved in neutrophil function and other immune-related processes such as B-cell differentiation and the JNK cascade within cluster 13. Within cluster 6, proteins involved in cell death, the cell cycle, morphogenesis, hedgehog signalling, collagen, and cytoskeletal organisation show increased abundance (Figure 6B).

MALDI imaging visualises lipid profiles that reflect immune cell infiltration

In addition to spatially mapping protein expression with the tissue, we also performed mass spectrometry imaging to investigate the spatial distribution of lipids within the tissue on an adjacent section using MALDI (Figure 6C). Bisecting K-means clustering of the MALDI imaging pixels derived from 498 molecular ions broadly reflects the proteomic and cluster maps' patterns, but with higher spatial resolution (20 µm). The upper-left region is a distinct cluster, and the boundary between the solid tumour and brain/tumour interface is visible. The ion image of haeme can be used as a proxy to visualise the vascularisation of the tissue. This also shows variability across the tissue, potentially indicating areas of nutrient gradients and availability in different regions of the solid tumour. Plotting the ion image of the 689.56 m/z ion that corresponds to the cholesterol ester[46] (18:1) $[M+K]^+$ ion shows the highest intensity in the region of the tissue that corresponds to the area of high macrophage marker expression (cluster 6) in the proteomic maps.

Discussion

The presented spatial analytics workflow addresses the need to generate highly multiplexed, quantitative, spatially resolved measurements of proteins within tissue to understand the spatial organisation of molecular pathways in health and pathology. We demonstrate methods for the systematic sampling of tissue sub-sections using laser capture microdissection (LCM), sample preparation, liquid chromatography-mass spectrometry and advanced statistical analysis of topographic data.

We optimised methodology to negotiate detected proteome depth versus spatial resolution (Figure S1) and demonstrate the detection of proteins and pathways with spatially variable abundance within a rare paediatric tumour - atypical teratoid/rhabdoid tumour – and surrounding tumour-infiltrated normal tissue. We applied spatially aware data analysis and statistics to pinpoint biological processes with deep molecular resolution without prior knowledge of the tissue composition, thus creating an objective, unbiased way of deep phenotyping pathological tissue in its biological context.

A growing number of studies are currently focused on feature-driven LCM-coupled proteomics. In contrast, here, we propose an unbiased, systematic approach, which allows the creation of comprehensive proteomic maps at the individual protein or pathway level. These maps can fulfil the requirements for feature-driven analysis by reconstituting features from systematic sampling and allow the discovery of new proteo-phenotypes without visually identifiable parameters. Furthermore, the method performs excellently compared to general high-sensitivity proteomic workflows for tissue analysis and other spatial proteomic methods performed in this resolution range.

Through our generation of proteomic maps, we have demonstrated the presence of molecular heterogeneity at multiple scales within tumour tissue sections, revealing proteomic differences between areas of tissue that appear visually homogeneous. These proteomic measurements show good agreement with immunohistochemistry staining of adjacent tissue sections. Additionally, we demonstrate that this approach can also generate information on immune cell infiltration and state within the tissue by the detection of neutrophil and pro-tumour M2 macrophage markers towards the periphery but at different distances from the solid tumour. In addition to characterising the proteomic spatial

heterogeneity across the tissue, we also show that the lipidomic fingerprint varies similarly and detect evidence of the same immune cell infiltration.

The work we present here has several avenues for future improvement to generate more comprehensive information about biological structures. Integrating multiple data modalities and patient data is critical to the complete understanding of disease processes, and the correct integration relies on advanced bioinformatics tools[47,48]. The full integration of spatially resolved proteomic, metabolic, lipidomic and transcriptomic data, along with high-resolution imaging, has the potential to reveal further insights into the spatial dimension of biological processes. Further development of data analysis and statistical methods that can use the spatial relationships between samples is also required to maximise the utility of spatially resolved proteomics. One aspect of this is the handling of missing values. The spatial information retained when the spatial context of samples is known could be used to aid data imputation methods capable of taking samples' spatial relationships into account[49,50].

However, the spatial resolution should be balanced with the expectation for a meaningful depth to cover pathways of interest and technical limitations for sensitivity and throughput. For example, an increase of spatial resolution towards the single-cell level (1-10um/pixel) with current LC-MS workflows would reduce the detected depth of the proteome to 100s of proteins, limiting the conclusions to be drawn about the fine spatial resolution of the proteome in such tissues. Several single-cell proteomic methods have been recently described, but they do not yet use cells collected by LCM[51–53]. Novel high-throughput LC-MS platforms can now robustly analyse 1000s of samples relatively quickly[54–56]. However, increasing the spatial resolution demonstrated here towards the single-cell level and covering comparable areas would be a formidable analytical challenge, further escalating when analysing tissue in three dimensions[57].

Another limitation is based on the samples analysed here still having properties of bulk tissue, but with a lower number of cells than usually analysed in bulk biopsies, even if mapped to physiological features or areas. This bulk property means that the data still suffers from missing values which can confound spatial pathway level analysis. Future approaches are bound to use systematic spatial proteomic analysis, possibly compromising spatial resolution but incorporating an element of machine learning to use orthogonal

higher resolution omics and imaging data to infer protein abundance towards individual cell resolution, as can be done on spatial transcriptomics data[58–61]. In addition, with the detection of LCM-based and cell-type resolved deep proteomes, these data will be highly complementary to current imaging technologies and increase the understanding of spatially resolved biological and pathological processes at the molecular level[29,32,57].

Acknowledgements

SD acknowledges support from the Nuffield Department of Medicine. SD, PDC, BMK & RF acknowledge support from the Chinese Academy of Medical Sciences Medical Sciences 2018-I2M-2-002. PDC was supported by Pfizer funding awarded to BMK.

We acknowledge the Oxford Brain Bank, supported by the Medical Research Council (MRC, MR/L022656/1) and Brains for Dementia Research (BDR) (Alzheimer Society and Alzheimer Research UK). This research project was funded by the NIHR Oxford Biomedical Research Centre (to OA, BRC-1215-20008). The views expressed are those of the authors and not necessarily those of the NHS, the NIHR, or the Department of Health. This work uses data provided by patients and collected by the NHS as part of their care and support and would not have been possible without access to this data. The NIHR recognises and values the role of patient data, securely accessed and stored, both in underpinning and leading to improvements in research and care.

Competing interests.

J.O is an employee of Bruker Daltonics GmbH & Co. KG. All other authors have no competing interests.

References

1. Asp, M. *et al.* A Spatiotemporal Organ-Wide Gene Expression and Cell Atlas of the Developing Human Heart. *Cell* **179**, 1647-1660.e19 (2019).

2. Baccin, C. *et al.* Combined single-cell and spatial transcriptomics reveal the molecular, cellular and spatial bone marrow niche organization. *Nat. Cell Biol.* **22**, 38–48 (2020).

3. Moncada, R. *et al.* Integrating microarray-based spatial transcriptomics and single-cell RNA-seq reveals tissue architecture in pancreatic ductal adenocarcinomas. *Nat. Biotechnol.* **38**, 333–342 (2020).

4. Shah, S., Lubeck, E., Zhou, W. & Cai, L. In Situ Transcription Profiling of Single Cells Reveals Spatial Organization of Cells in the Mouse Hippocampus. *Neuron* **92**, 342–357 (2016).

5. Thrane, K., Eriksson, H., Maaskola, J., Hansson, J. & Lundeberg, J. Spatially resolved transcriptomics enables dissection of genetic heterogeneity in stage III cutaneous malignant melanoma. *Cancer Res.* **78**, 5970–5979 (2018).

6. Berglund, E. *et al.* Spatial maps of prostate cancer transcriptomes reveal an unexplored landscape of heterogeneity. *Nat. Commun.* **9**, 1–13 (2018).

7. Keren, L. *et al.* A Structured Tumor-Immune Microenvironment in Triple Negative Breast Cancer Revealed by Multiplexed Ion Beam Imaging. *Cell* **174**, 1373–1387 (2018).

8. Farahbod, M. & Pavlidis, P. Untangling the effects of cellular composition on coexpression analysis. *Genome Res.* **30**, 849–859 (2020).

9. Bloom, A. B. & Zaman, M. H. Influence of the microenvironment on cell fate determination and migration. *Physiological Genomics* vol. 46 309–314 (2014).

10. De Palma, M., Biziato, D. & Petrova, T. V. Microenvironmental regulation of tumour angiogenesis. *Nature Reviews Cancer* vol. 17 457–474 (2017).

11. Balkwill, F. R., Capasso, M. & Hagemann, T. The tumor microenvironment at a glance. *J. Cell Sci.* **125**, 5591–5596 (2012).

12. Karczewski, K. J. & Snyder, M. P. Integrative omics for health and disease. *Nat. Rev. Genet.* **19**, 299–310 (2018).

13. Wang, Z., Gerstein, M. & Snyder, M. RNA-Seq: A revolutionary tool for transcriptomics. *Nature Reviews Genetics* vol. 10 57–63 (2009).

14. Goodwin, S., McPherson, J. D. & McCombie, W. R. Coming of age: Ten years of next-generation sequencing technologies. *Nat. Rev. Genet.* **17**, 333–351 (2016).

15. Mamlouk, S. *et al.* DNA copy number changes define spatial patterns of heterogeneity in colorectal cancer. *Nat. Commun.* **8**, 14093 (2017).

16. Marek, S. *et al.* Spatial and Temporal Organization of the Individual Human Cerebellum. *Neuron* **100**, 977–993 (2018).

17. Aebersold, R. & Mann, M. Mass-spectrometric exploration of proteome structure and function. *Nature* **537**, 347–355 (2016).

18. Caprioli, R. M., Farmer, T. B. & Gile, J. Molecular Imaging of Biological Samples: Localization of Peptides and Proteins Using MALDI-TOF MS. *Anal. Chem.* **69**, 4751–4760 (1997).

19. Todd, P. J., Gregory Schaaff, T., Chaurand, P. & Caprioli, R. M. Organic ion imaging of biological tissue with secondary ion mass spectrometry and matrix-assisted laser desorption/ionization. *J. Mass Spectrom.* **36**, 355–369 (2001).

20. Angelo, M. *et al.* Multiplexed ion beam imaging of human breast tumors. *Nat. Med.* **20**, 436–442 (2014).

21. Giesen, C. *et al.* Highly multiplexed imaging of tumor tissues with subcellular resolution by mass cytometry. *Nat. Methods* **11**, 417–422 (2014).

22. Kertesz, V. & Van Berkel, G. J. Fully automated liquid extraction-based surface sampling and ionization using a chip-based robotic nanoelectrospray platform. *J. Mass Spectrom.* **45**, 252–260 (2010).

23. Ryan, D. J. *et al.* Protein identification in imaging mass spectrometry through spatially targeted liquid micro-extractions. *Rapid Commun. Mass Spectrom.* **32**, 442–450 (2018).

24. De Marchi, T. *et al.* The advantage of laser-capture microdissection over whole tissue analysis in proteomic profiling studies. *Proteomics* **16**, 1474–1485 (2016).

25. Zhu, Y. *et al.* Spatially Resolved Proteome Mapping of Laser Capture Microdissected Tissue with Automated Sample Transfer to Nanodroplets. *Mol. Cell. Proteomics* **17**, 1864–1874 (2018).

26. Buczak, K. *et al.* Spatial tissue proteomics quantifies inter- and intratumor heterogeneity in hepatocellular carcinoma (HCC). *Mol. Cell. Proteomics* **17**, 810–825 (2018).

27. Longuespée, R. *et al.* A laser microdissection-based workflow for FFPE tissue microproteomics: Important considerations for small sample processing. *Methods* **104**, 154–162 (2016).

28. Zhu, Y. *et al.* Development of a laser capture microscope-based single-cell-type proteomics tool for studying proteomes of individual cell layers of plant roots. *Hortic. Res.* **3**, (2016).

29. Davis, S., Scott, C., Ansorge, O. & Fischer, R. Development of a Sensitive, Scalable Method for Spatial, Cell-Type-Resolved Proteomics of the Human Brain. *J. Proteome Res.* **18**, 1787–1795 (2019).

30. Coscia, F. *et al.* A streamlined mass spectrometry–based proteomics workflow for large-scale FFPE tissue analysis. *J. Pathol.* **251**, 100–112 (2020).

31. Griesser, E. *et al.* Quantitative Profiling of the Human Substantia Nigra Proteome from Laser-capture Microdissected FFPE Tissue. *Mol. Cell. Proteomics* **19**, 839–851 (2020).

32. Mund, A. *et al.* AI-driven Deep Visual Proteomics defines cell identity and heterogeneity. *bioRxiv* 2021.01.25.427969 (2021) doi:10.1101/2021.01.25.427969.

33. Waanders, L. F. *et al.* Quantitative proteomic analysis of single pancreatic islets. *Proc. Natl. Acad. Sci. U. S. A.* **106**, 18902–7 (2009).

34. Clair, G. *et al.* Spatially-Resolved Proteomics: Rapid Quantitative Analysis of Laser Capture Microdissected Alveolar Tissue Samples. *Sci. Rep.* **6**, 39223 (2016).

35. Eckert, M. A. *et al.* Proteomics reveals NNMT as a master metabolic regulator of cancer-associated fibroblasts. *Nature* **569**, 723–728 (2019).

36. Herrera, J. A. *et al.* Laser capture microdissection coupled mass spectrometry (LCM-MS) for spatially resolved analysis of formalin-fixed and stained human lung tissues. *Clin. Proteomics* **17**, 24 (2020).

37. Piehowski, P. D. *et al.* Automated mass spectrometry imaging of over 2000 proteins from tissue sections at 100-µm spatial resolution. *Nat. Commun.* **11**, 1–12 (2020).

38. Favaro, E. *et al.* Glucose Utilization via Glycogen Phosphorylase Sustains Proliferation and Prevents Premature Senescence in Cancer Cells. *Cell Metab.* **16**, 751–764 (2012).

39. Porlier, M. M., de Néchaud, B. & Gros, F. Peripherin, a new member of the intermediate filament protein family. *Dev. Neurosci.* **6**, 335–344 (1983).

40. Yuan, A. *et al.* Peripherin is a subunit of peripheral nerve neurofilaments: Implications for differential vulnerability of cns and peripheral nervous system axons. *J. Neurosci.* **32**, 8501–8508 (2012).

41. Troy, C. M., Brown, K., Greene, L. A. & Shelanski, M. L. Ontogeny of the neuronal intermediate filament protein, peripherin, in the mouse embryo. *Neuroscience* **36**, 217–237 (1990).

42. Moran, P. A. P. Notes on Continuous Stochastic Phenomena. *Biometrika* **37**, 17–23 (1950).

43. Langfelder, P., Zhang, B. & Horvath, S. Defining clusters from a hierarchical cluster tree: The Dynamic Tree Cut package for R. *Bioinformatics* **24**, 719–720 (2008).

44. Orecchioni, M., Ghosheh, Y., Pramod, A. B. & Ley, K. Macrophage Polarization: Different Gene Signatures in M1(LPS+) vs. Classically and M2(LPS–) vs. Alternatively Activated Macrophages. *Front. Immunol.* **10**, (2019).

45. Hu, J. M. *et al.* CD163 as a marker of M2 macrophage, contribute to predict aggressiveness and prognosis of Kazakh esophageal squamous cell carcinoma. *Oncotarget* **8**, 21526–21538 (2017).

46. Guerrini, V. & Gennaro, M. L. Foam Cells: One Size Doesn't Fit All. *Trends Immunol.*

40, 1163–1179 (2019).

47. Santos, A. *et al.* A knowledge graph to interpret clinical proteomics data. *Nat. Biotechnol.* (2022) doi:10.1038/s41587-021-01145-6.

48. Subramanian, I., Verma, S., Kumar, S., Jere, A. & Anamika, K. Multi-omics Data Integration, Interpretation, and Its Application. *Bioinform. Biol. Insights* **14**, (2020).

49. Li, Z., Song, T., Yong, J. & Kuang, R. Imputation of spatially-resolved transcriptomes by graph-regularized tensor completion. *PLoS Comput. Biol.* **17**, e1008218 (2021).

50. Boluki, S., Zamani Dadaneh, S., Qian, X. & Dougherty, E. R. Optimal clustering with missing values. *BMC Bioinformatics* **20**, 1–10 (2019).

51. Specht, H. *et al.* Single-cell proteomic and transcriptomic analysis of macrophage heterogeneity using SCoPE2. *Genome Biol.* **22**, 50 (2021).

52. Brunner, A. *et al.* Ultra-high sensitivity mass spectrometry quantifies single-cell proteome changes upon perturbation. *Mol. Syst. Biol.* **18**, (2022).

53. Ctortecka, C. *et al.* An automated workflow for multiplexed single-cell proteomics sample preparation at unprecedented sensitivity. *bioRxiv* (2022) doi:10.1101/2021.04.14.439828.

54. Bache, N. *et al.* A novel LC system embeds analytes in pre-formed gradients for rapid, ultra-robust proteomics. *Mol. Cell. Proteomics* **17**, 2284–2296 (2018).

55. Bian, Y. *et al.* Robust, reproducible and quantitative analysis of thousands of proteomes by micro-flow LC–MS/MS. *Nat. Commun.* **11**, 1–12 (2020).

56. Messner, C. B. *et al.* Ultra-fast proteomics with Scanning SWATH. *Nat. Biotechnol.* **39**, 846–854 (2021).

57. Bhatia, H. S. *et al.* Proteomics of spatially identified tissues in whole organs. *bioRxiv* (2021) doi:10.1101/2021.11.02.466753.

58. Pang, M., Su, K. & Li, M. Leveraging information in spatial transcriptomics to predict super-resolution gene expression from histology images in tumors. *bioRxiv* 2021.11.28.470212 (2021) doi:10.1101/2021.11.28.470212.

59. Monjo, T., Koido, M., Nagasawa, S., Suzuki, Y. & Kamatani, Y. Efficient prediction of a spatial transcriptomics profile better characterizes breast cancer tissue sections without costly experimentation. *Sci. Rep.* **12**, 4133 (2022).

60. Bergenstråhle, L. *et al.* Super-resolved spatial transcriptomics by deep data fusion. *Nat. Biotechnol.* (2021) doi:10.1038/s41587-021-01075-3.

61. He, B. *et al.* Integrating spatial gene expression and breast tumour morphology via deep learning. *Nat. Biomed. Eng.* **4**, 827–834 (2020).

62. Hughes, C. S. *et al.* Ultrasensitive proteome analysis using paramagnetic bead technology. *Mol. Syst. Biol.* **10**, 757 (2014).

63. Sielaff, M. *et al.* Evaluation of FASP, SP3 and iST Protocols for Proteomic Sample Preparation in the Low Microgram Range. *J. Proteome Res.* **16**, 4060–4072 (2017).

64. Sandow, J., Infusini, G., Dagley, L., Larsen, R. & Webb, A. Simplified high-throughput methods for deep proteome analysis on the timsTOF Pro. *bioRxiv* 657908 (2019) doi:10.1101/657908.

65. Cox, J. *et al.* Accurate Proteome-wide Label-free Quantification by Delayed Normalization and Maximal Peptide Ratio Extraction, Termed MaxLFQ. *Mol. Cell. Proteomics* **13**, 2513–2526 (2014).

66. Tyanova, S., Temu, T. & Cox, J. The MaxQuant computational platform for mass spectrometry-based shotgun proteomics. *Nat. Protoc.* **11**, 2301–2319 (2016).

67. Bivand, R. S. & Wong, D. W. S. Comparing implementations of global and local indicators of spatial association. *TEST* **27**, 716–748 (2018).

68. Bivand, R. S., Pebesma, E. J., Gomez-Rubio, V. & Pebesma, E. J. *Applied spatial data analysis with R*. vol. 2 (Springer, 2013).

69. Hijmans, R. J. raster: Geographic Data Analysis and Modeling. (2020).

70. McInnes, L., Healy, J., Saul, N. & Großberger, L. UMAP: Uniform Manifold Approximation and Projection. *J. Open Source Softw.* **3**, 861 (2018).

71. Yu, G., Wang, L.-G., Han, Y. & He, Q.-Y. clusterProfiler: an R Package for Comparing

Biological Themes Among Gene Clusters. *Omi. A J. Integr. Biol.* **16**, 284–287 (2012).

72. Deutskens, F., Yang, J. & Caprioli, R. M. High spatial resolution imaging mass spectrometry and classical histology on a single tissue section. *J. Mass Spectrom.* **46**, 568–571 (2011).

73. Ly, A. *et al.* Site-to-Site Reproducibility and Spatial Resolution in MALDI–MSI of Peptides from Formalin-Fixed Paraffin-Embedded Samples. *Proteomics - Clin. Appl.* **13**, 1800029 (2019).

Methods

Tissue retrieval and processing

Post-mortem brain tissue was retrieved by the Oxford Brain Bank; a research ethics committee (REC) approved and HTA regulated research tissue bank (REC reference 15/SC/0639). The retrieved brain was sectioned into 1 cm thick coronal sections starting at the level of the mammillary bodies. Due to its large size, tumour tissue was present within multiple of these coronal slices. The tumour tissue was dissected from the first coronal and second posterior coronal slices (P1 and P2). The tumour from the P2 slice was split into quadrants. Cryosections were taken from all pieces to determine the tissue block with the best morphological and cellular preservation. Cryosections were stained with H&E (see below) and examined by a Neuropathologist (OA). The upper-right quadrant from the P2 coronal slice was selected for use in further experiments.

Relevant tissue blocks of the AT/RT tumour were acclimatised to -20 °C and mounted onto a cryostat block using OCT Compound (Cell Path, ARG1180). Careful consideration was taken to ensure cut sections were not contaminated with OCT. Sections were cut at 10 µm and mounted onto UV irradiated (254 nm, 30 minutes) 1.0 PEN membrane slides (Zeiss) at -18 °C for LCM or Superfrost glass slides for histology. Sections were then air-dried for several minutes and placed onto a Shandon Linistain for automated H&E staining. Sections were fixed in 70 % denatured alcohol, hydrated, stained with Harris' Haematoxylin, incubated in 0.4 % acid alcohol, placed in Scot's tap water, and stained with Eosin containing 0.25 % acetic acid with regular washing steps in between. Stained sections were then dehydrated in increasing concentrations of denatured alcohol and air-dried without coverslips and stored at -80 °C until processing by laser-capture microdissection.

Laser capture microdissection

Areas of tissue analysed were annotated and isolated from the prepared slides using a laser-capture microscope equipped with laser pressure catapulting (PALM Microbeam, Zeiss). Cutting and capturing the annotated tissue areas were performed automatically and used the 10x objective lens. The settings in the control software for cutting were Energy: 43, Focus: 55; and for capturing were Energy 20, Focus -15. Samples were collected into 20 µL

RIPA buffer (Pierce #89900) in the cap of 200 µL PCR tubes or PCR-cap strips of 8. Collected samples were immediately placed in dry ice. Samples were stored at -80 °C until further use.

Proteomic sample processing

Samples were thawed, incubated at room temperature for 30 minutes and briefly centrifuged. Caps were rinsed with 20 µL of RIPA buffer (#89900, Pierce) containing 25 units of Benzonase (E1014, Merck) to collect any remaining tissue and briefly centrifuged, followed by incubation at room temperature for 30 minutes to degrade DNA and RNA. Proteins were reduced by adding DTT to 5 mM and incubated at room temperature for 30 minutes, followed by the addition of iodoacetamide to 20 mM and incubation at room temperature for 30 minutes.

Paramagnetic SP3 beads (GE45152105050250 & GE65152105050250, Cytiva) were prepared as described by Hughes *et al.* and processed by a modified SP3 protocol [29,62,63]. Three µL of SP3 beads were mixed with the samples, and acetonitrile added to a final concentration of 70 % (v/v). Samples were mixed with 1000 rpm orbital shaking for 18 minutes, followed by bead immobilisation on a magnet for 2 minutes. The supernatant was discarded, and beads were washed twice with 70 % (v/v) ethanol in water and once with 100 % acetonitrile without removal from the magnet. Beads were resuspended in 50 mM ammonium bicarbonate containing 25 ng of Trypsin (V5111, Promega) and digested overnight at 37 °C. After digestion, the beads were resuspended by bath sonication. Acetonitrile was added to the samples to 95 % (v/v) and shaken at 1000 rpm for 18 minutes. Beads were immobilised on a magnet for 2 minutes, and the supernatant discarded. Beads were resuspended in 2 % acetonitrile and immobilised on a magnet for 5 minutes. Peptides were transferred to glass LC-MS vials or 96-well PCR plates containing formic acid in water, resulting in a final formic acid concentration of 0.1 %.

LC-MS/MS

Peptides from 833 µm resolution samples were analysed by LC-MS/MS using a Dionex Ultimate 3000 (Thermo Scientific) coupled to a timsTOF Pro (Bruker) using a 75 µm x 150 mm C18 column with 1.6 µm particles (IonOpticks) at a flow rate of 400 nL/min. A 17-minute linear gradient from 2 % buffer B to 30 % buffer B (A: 0.1 % formic acid in water. B: 0.1 % formic acid in acetonitrile) was used[64]. The TimsTOF Pro was operated in PASEF mode.

The TIMS accumulation and ramp times were set to 100 ms, and mass spectra were recorded from 100 – 1700 m/z, with a 0.85 – 1.30 Vs/cm2 ion mobility range. Precursors were selected for fragmentation from an area of the full TIMS-MS scan that excludes most ions with a charge state of 1+. Those selected precursors were isolated with an ion mobility dependent collision energy, increasing linearly from 27 – 45 eV over the ion mobility range. Three PASEF MS/MS scans were collected per full TIMS-MS scan, giving a duty cycle of 0.53 s. Ions were included in the PASEF MS/MS scan if they met the target intensity threshold of 2000 and were sampled multiple times until a summed target intensity of 10000 was reached. A dynamic exclusion window of 0.015 m/z by 0.015 Vs/cm2 was used, and sampled ions were excluded from reanalysis for 24 seconds.

Peptides from 350 µm resolution samples were analysed by nano-UPLC-MS/MS using a Dionex Ultimate 3000 coupled to an Orbitrap Fusion Lumos (Thermo Scientific) using a 75 µm x 500 mm C18 EASY-Spray Columns with 2 µm particles (Thermo Scientific) at a flow rate of 250 nL/min. A 60-minute linear gradient from 2 % buffer B to 35 % buffer B (A: 5 % DMSO, 0.1 % formic acid in water. B: 5 % DMSO, 0.1 % formic acid in acetonitrile). MS1 scans were acquired in the Orbitrap between 400 and 1500 m/z with a resolution of 120,000 and an AGC target of 4×10^5. Precursor ions between charge state 2+ and 7+ and above the intensity threshold of 5×10^3 were selected for HCD fragmentation at a normalised collision energy of 28 %, an AGC target of 4×10^3, a maximum injection time of 80 ms and a dynamic exclusion window of 30 s. MS/MS spectra were acquired in the ion trap using the rapid scan mode.

Proteomic data analysis

Raw data files were searched against the Uniprot human database (Retrieved 17/01/2017, 92527 sequences) using MaxQuant version 1.6.14.0, allowing for tryptic specificity with up to 2 missed cleavages. Cysteine carbamidomethylation was set as a fixed modification. Methionine oxidation and protein N-terminal acetylation were set as variable modifications and the “match between runs (MBR)” option was used (MBR was not used for tissue titration data). All other settings were left as default. Label-free quantification was performed using the MaxLFQ algorithm within MaxQuant[65,66]. Protein and peptide false discovery rate (FDR) levels were set to 1 %.

Spatial data analysis

The spatial analysis uses functions within the spdep and raster R packages[67–69]. MaxQuant's protein level output files ('proteingroups.txt') were filtered to remove reverse hits, 'Only identified by site' hits and potential contaminants. The 'LFQ intensity' columns were $\log_2$ transformed and then normalised by median subtraction. Protein groups that did not meet a cut-off of having at least 9 pixels with normalised LFQ values are not taken forward for further analysis. The following steps occur independently for each protein group. Normalised LFQ intensities were then coerced into a matrix reflecting the rastered pattern of sample acquisition. The quantification matrix was converted into a raster object and then to a polygon object using the raster R package. From this polygon object, a neighbour list was built for each pixel of the raster using the 'Queen's Case' where cells are considered neighbours if they share an edge or a vertex. The neighbour list was then supplemented with a spatial weights matrix using a binary coding scheme where neighbours are given a weighting of '1' and non-neighbours a weighting of '0' in the spatial weights matrix. The raster object and the weighted neighbour list were then used as inputs to a permutation test for the Moran's *I* statistic, calculated using 999 random spatial permutations of the raster object to calculate pseudo-*p*-values. Moran's *I* statistics and the associated *p*-values are collected for every protein group. The *p*-values were then corrected for multiple testing using the Benjamini-Hochberg FDR method.

Immunohistochemistry

Sections were cut as above and were mounted to superfrost glass slides for IHC and air-dried. Slides were fixed in ice-cold acetone for 10 minutes, washed twice with TBS/T (20 mM Tris, 150 mM NaCl, 0.05 % Tween 20) and blocked with 10 % goat serum in TBS/T for 60 minutes at room temperature. Primary antibodies were diluted in 5 % goat serum in TBS/T and incubated at RT for 60 minutes or 4 °C overnight. Sections were washed three times with TBS/T. Staining visualisation was performed by incubating with a cocktail of anti-mouse and anti-rabbit secondary antibodies conjugated to horseradish peroxidase (Envision Kit, Agilent) for 60 minutes at room temperature. Sections were then washed with TBS/T three times and incubated with 2 % 3,3'-diaminobenzidine for 5 minutes, immersed in water and then counterstained with Harris' Haematoxylin for 1 minute. Primary antibodies used and dilutions: rabbit anti-PYGL, 1:100, 4 °C overnight, HPA000962 (Atlas Antibodies); rabbit anti-

ASPH, 1:1000, RT 60 minutes, NBP2-34125 (Novus Biologicals); mouse anti-CD45 (PD7/26 + 2B11), 1:200, RT 60 minutes, ab781 (Abcam).

Clustering

Empty pixels and pixels covering the large region of haemorrhage were not included. A distance matrix was built containing the Euclidean distance between each pixel's set of protein LFQ values. Hierarchical clustering of the distance matrix was performed in R using the "average" agglomeration method. Dendrograms were cut using the Dynamic Tree Cut method at a height setting of 100[43].

A complete input matrix is required for UMAP visualisation[70], so proteins with fewer than 70 % valid values across the experiment were removed. The remaining missing values were imputed in on a per-sample basis by random draws from a normal distribution using a width of 0.3 and a downshift of 1.8. UMAP dimensionality reduction was performed on this imputed data with default settings, and the first two embedding components plotted, and samples coloured according to their cluster assigned by Dynamic Tree Cut at a height of 100.

Pathway Analysis

A one-way ANOVA test was performed in R to test for differences in means between the clusters generated by Dynamic Tree Cut at a height of 100. A pairwise post-hoc correction was applied using Tukey's Honestly Significant Difference method. The resulting pairwise comparisons were used as inputs to ClusterProfiler's gene set enrichment analysis to test for enrichment of Gene Ontology Biological Process terms using a Fisher's exact test with a 5 % FDR threshold[71].

Lipid MALDI imaging

Vacuum dried sections were washed according to a Carnoy procedure as described in Deutskens et al. and dried again under vacuum for at least 30 min[72]. The slides were scanned with a TissueScout scanner at 3200 dpi (Bruker) to generate a reference image for later position teaching. Trypsin was applied using a TM-sprayer (HTX Technologies) as described in Ly et al. and digested for 2 h at 50 °C[73]. Dihydroxybenzoic acid (DHB) was dissolved at a concentration of 15 mg/ml in 90 % ACN, 0.1 % TFA and sprayed on top of the AT/RT sections using a TM-sprayer (HTX Technologies). The matrix was applied in a criss-cross pattern with 3 mm track spacing at a 1200 mm/min nozzle velocity. Fourteen layers

were sprayed at a 0.125 ml/ml flow rate using 50 % ACN as the liquid phase at 10 psi pressure. The nozzle temperature was set to 60 °C and the distance of the nozzle to the section was 40 mm. All imaging data were acquired on a timsTOF fleX instrument (Bruker) which is equipped with a dual ESI and MALDI source in positive Q-TOF mode. External calibration was performed using red phosphorous which was spotted next to the section. The laser was operated in beam scan mode, ablating an area of 15x15 µm resulting in a pixel size of 20 µm. The repetition rate of the laser was set to 10 kHz and 400 laser shots were acquired per pixel. Data were acquired in the mass range 300-1400 m/z.

The software SCiLS Lab (version 2020a; Bruker) was used for MALDI Imaging data analysis. All data were root-mean-square (RMS) normalised. After importing the data, an unsupervised segmentation was calculated using the bisecting k-means algorithm and a peak list containing 302 m/z-intervals with correlation used as a distance metric. The resulting segmentation map was split into several clusters that resemble the histopathology of the tumour section.

Data availability

The mass spectrometry proteomics data will be deposited to the ProteomeXchange Consortium via the PRIDE partner repository and made available to reviewers upon submission.

Figures

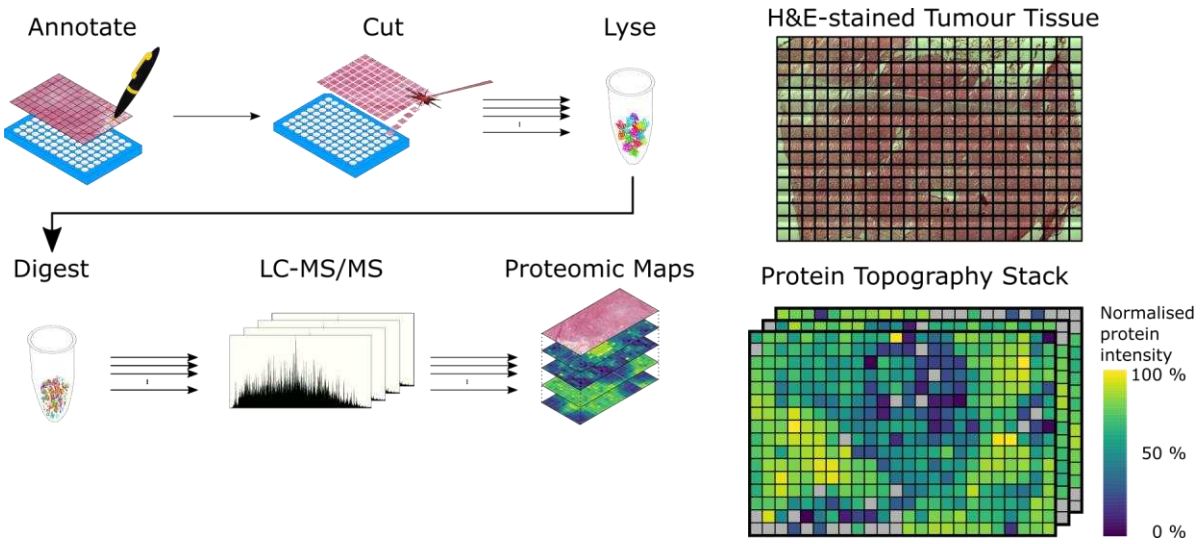

Figure 1 – Overview of the spatially resolved proteomics workflow
Tissue is segmented into a regular grid shape, and each element of the grid is isolated by laser capture microdissection (LCM). Proteins from each individually lysed sample are digested before analysis by LC-MS/MS. The quantitative information for each protein can be mapped back to its location within the gridded tissue and visualised in a topographic protein map, with one map per protein quantified.

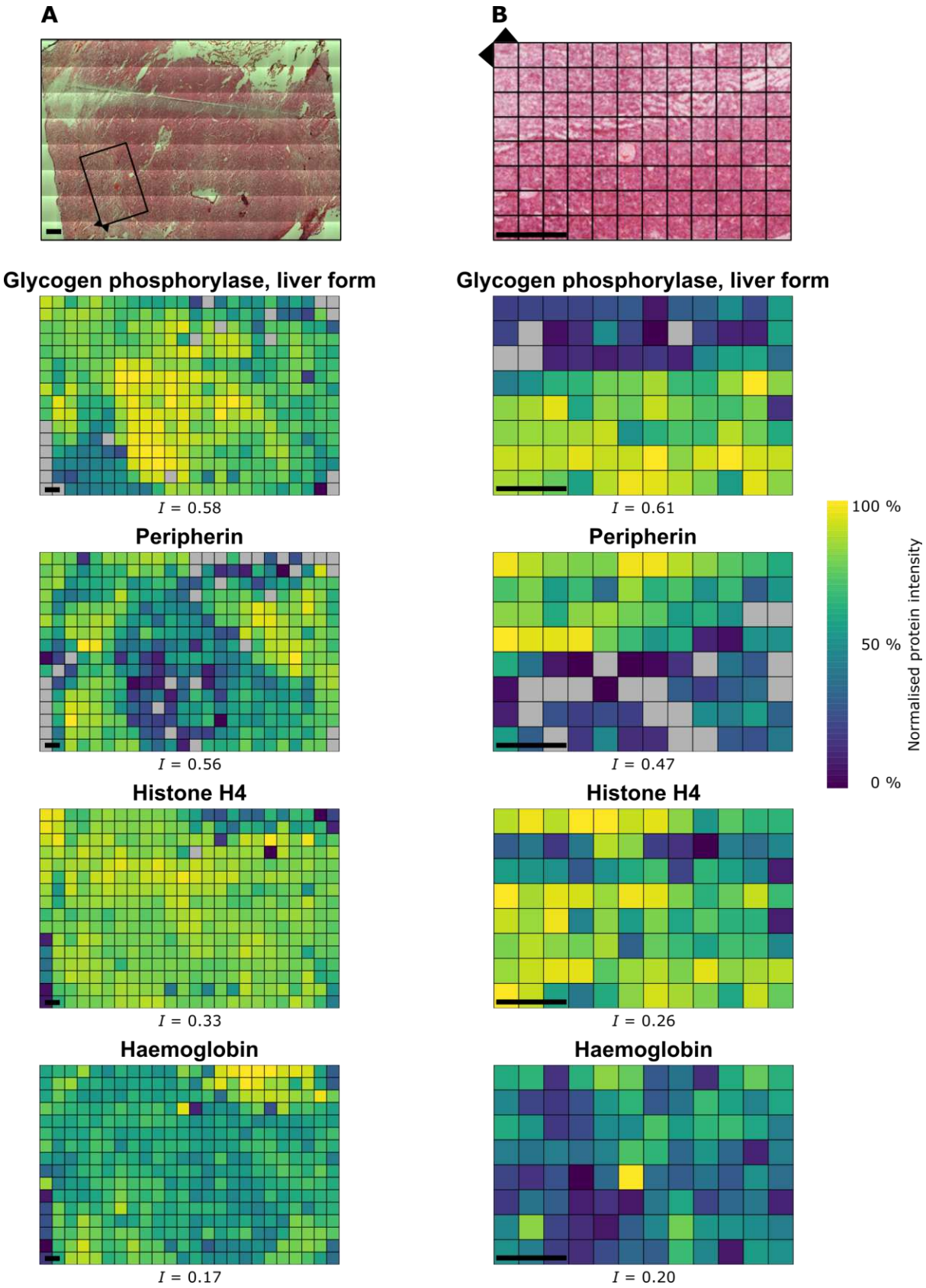

Figure 2 – Spatial proteomic maps of AT/RT tumour tissue

Normalised protein intensity of four example proteins mapped back to the original spatial positions within the atypical teratoid-rhabdoid tumour (AT/RT) tumour tissue at a resolution

of 833 µm (A) and 350 µm (B) with their corresponding Moran's Index of spatial autocorrelation (*I*). Box in (A) represents the area analysed in an adjacent tissue section (B). Scale bar = 1 mm. Normalised protein intensities are scaled separately for each protein. Gray = missing value.

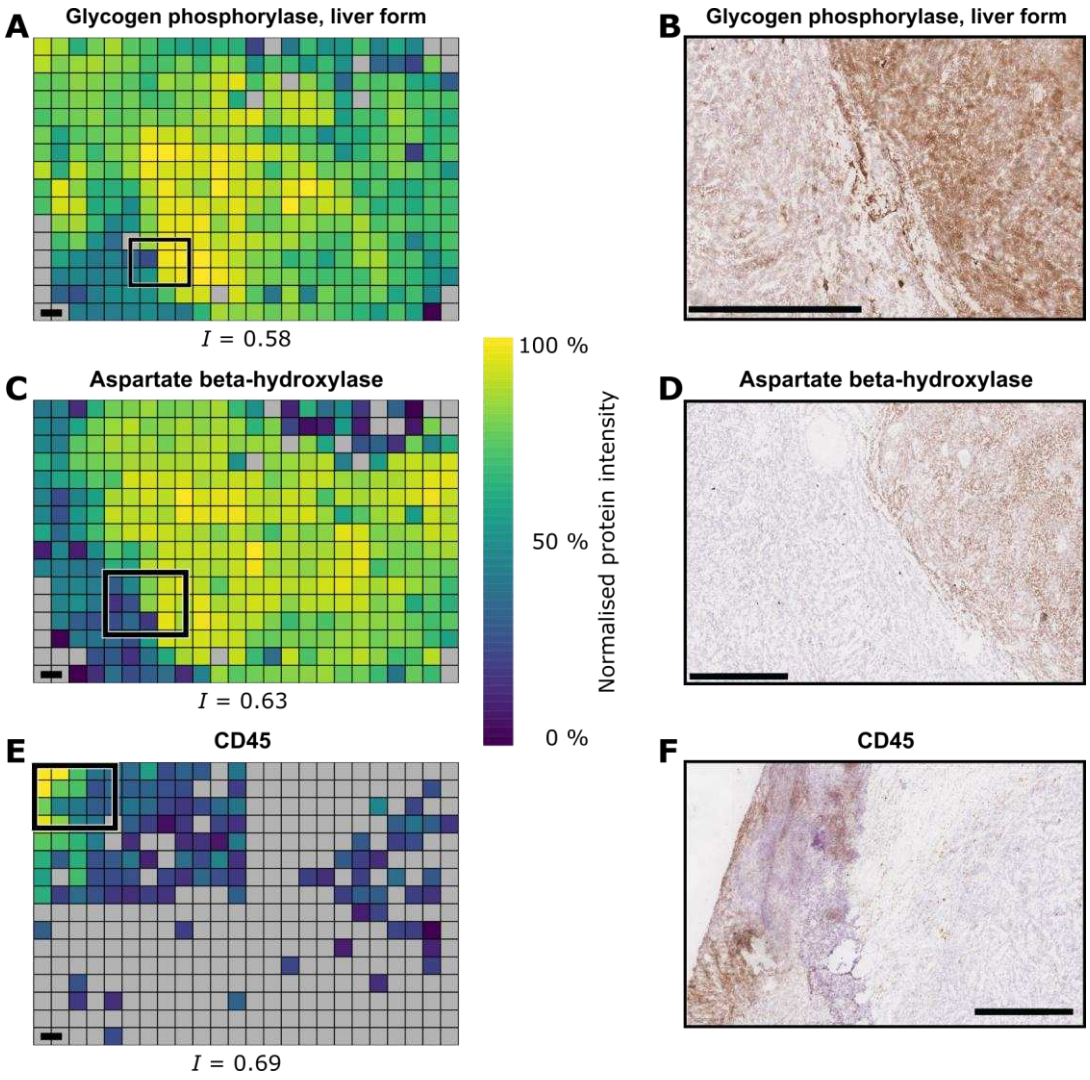

Figure 3 - Immunohistochemistry validation of AT/RT proteomic maps
Proteomic maps of proteins targeted for follow-up IHC staining and IHC images. (A,C,E) Normalised protein intensity maps with their corresponding Moran's Index of spatial autocorrelation (*I*). Normalised protein intensities are scaled separately for each protein. Gray = not quantified. Rectangles depict the approximate location displayed in IHC images. (B,D,F) AT/RT tissue stained and visualised by IHC. All scale bars = 1 mm.

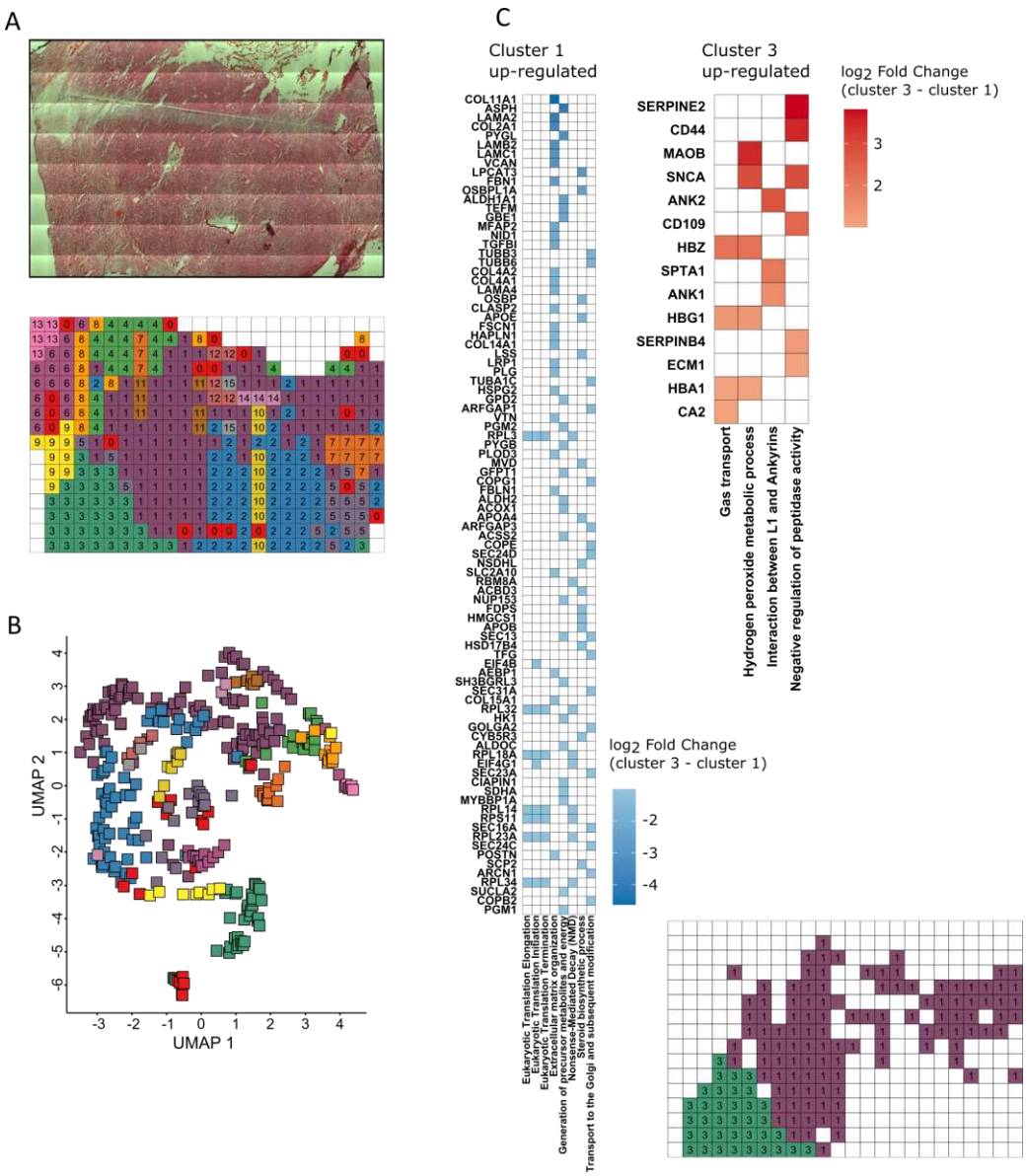

Figure 4 - Clustering and functional analysis of AT/RT proteomic maps

(A) Map of cluster assignment based on hierarchical clustering and the dynamic tree cut algorithm. White pixels represent excluded empty regions and regions of haemorrhage (B) UMAP embedding of data coloured by cluster assignment in (A). (C) GSEA of clusters 1 & 3 from (A). Gene set membership is indicated by colouring the cell with that protein's $\log_2$ fold-change.

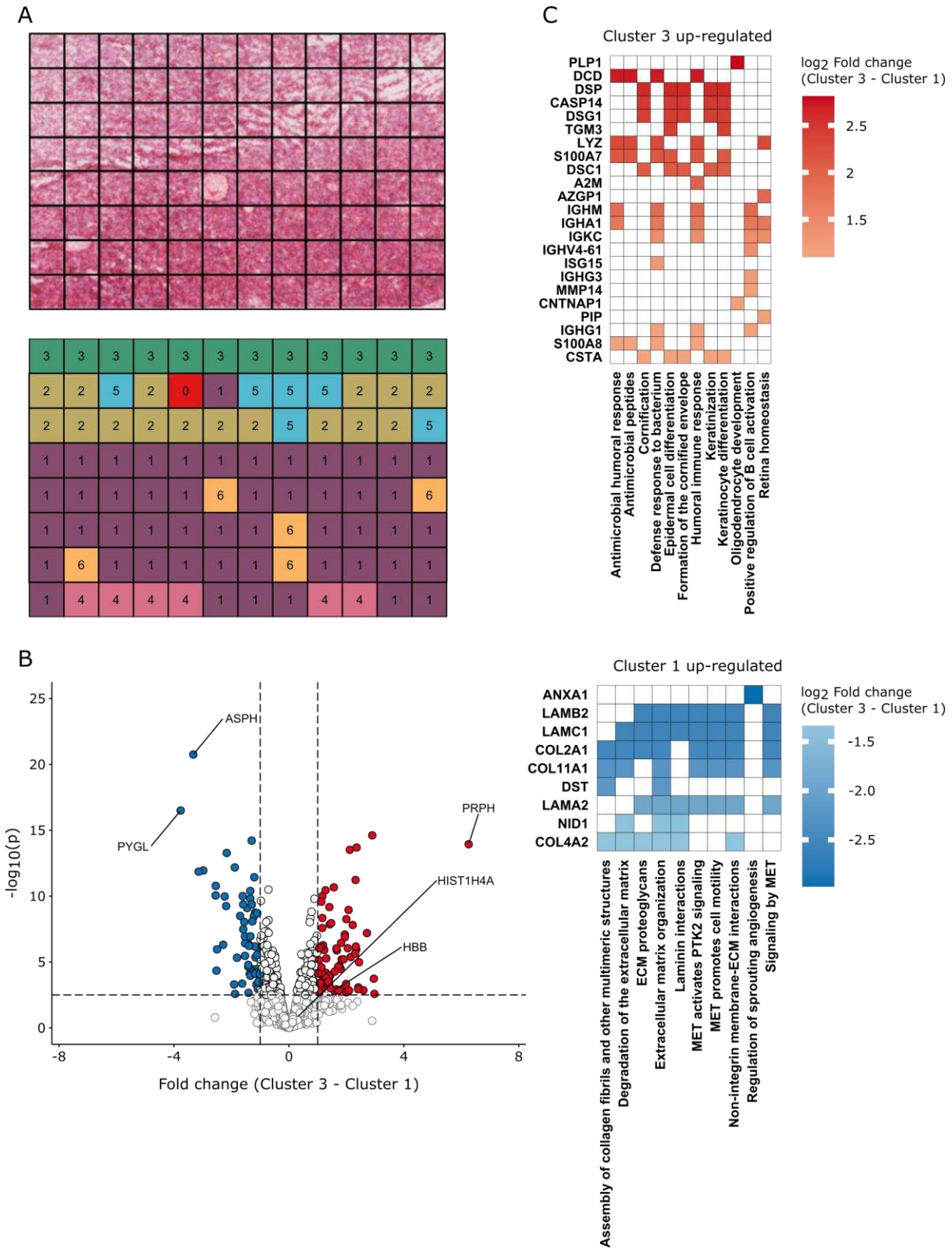

Figure 5 - High-resolution proteomic map clustering

(A) Map of cluster assignment based on hierarchical clustering and the dynamic tree cut algorithm. Cluster 3 corresponds to brain/tumour interface. Cluster 1 corresponds to solid tumour. Clusters 2 & 5 correspond to the transition between solid tumour and brain/tumour interface (B) Volcano plot of clusters 3 against cluster 1 from (A). The

horizontal dashed line represents an FDR of 5 %. The vertical dashed line represents -/+ 2-fold-change. (C) GSEA of clusters 1 & 3 from (A). Gene set membership is indicated by colouring the cell with that protein's $\log_2$ fold-change.

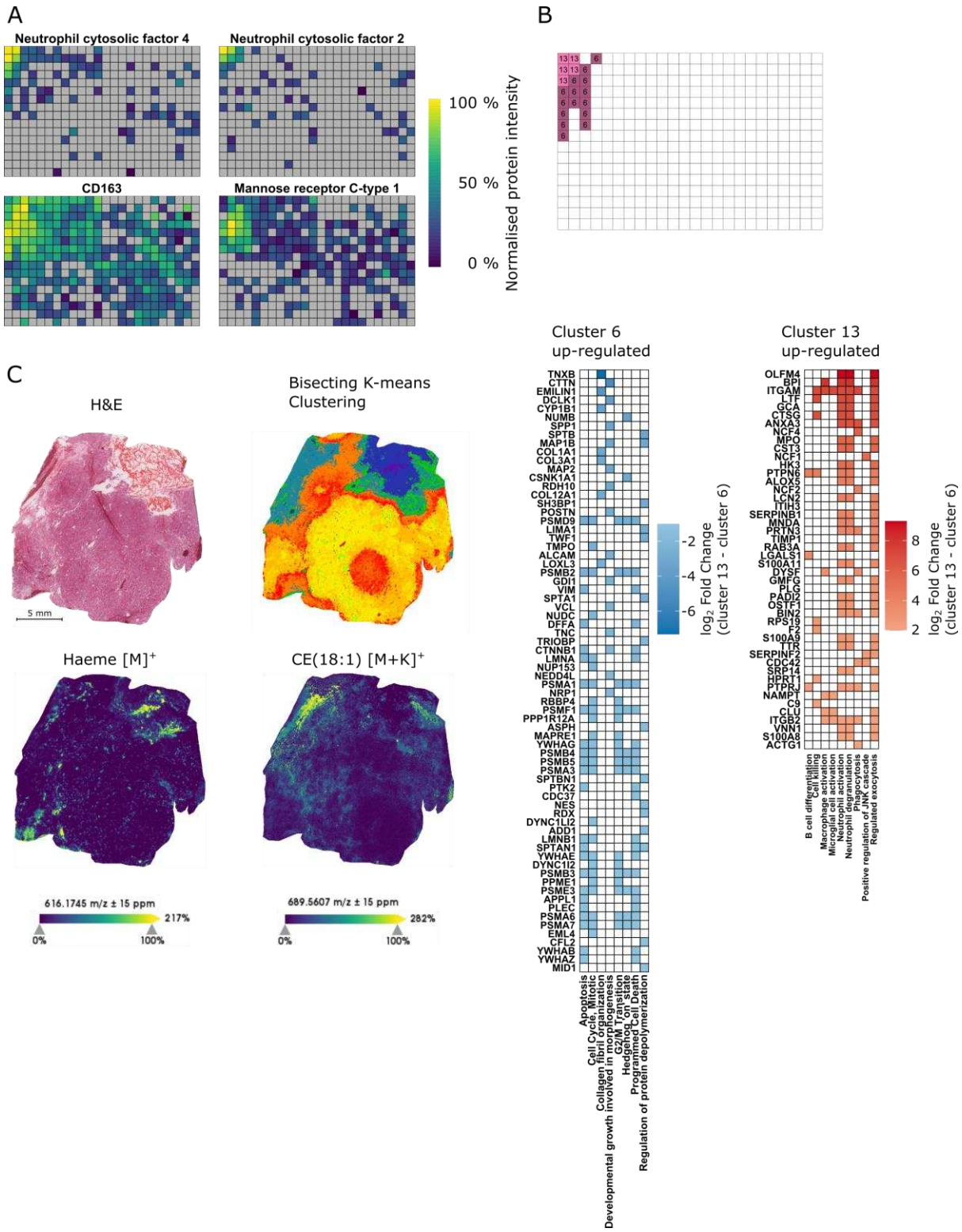

Figure 6 - Immune cell infiltration and lipid heterogeneity in AT/RT brain tumour
(A) Proteomic maps of immune cell-marker proteins at 833 µm resolution. Normalised protein intensities are scaled separately for each protein. (B) GSEA of clusters 6 & 13 from Figure 4A. Gene set membership is indicated by colouring the cell with that protein's log2 fold-change. (C) MALDI imaging of AT/RT lipids at 20 µm resolution. H&E image acquired after MALDI imaging (upper left) Bisecting K-means clusters of MALDI imaging pixels are indicated by colour (upper right). m/z images for ions corresponding to the mass of haeme

(bottom left) and cholesterol ester (18:1) (bottom right). Ion intensities are scaled separately for each ion.

Supplementary Figures

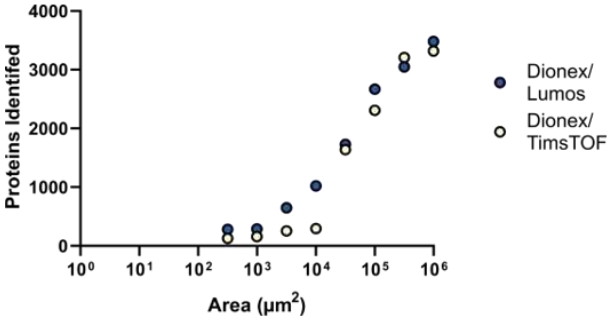

	Side Length (μm)	Area (μm²)	cells
$10^{2.5}$	18	316	2.7
10^3	32	1,000	8.6
$10^{3.5}$	56	3,162	27
10^4	100	10,000	86
$10^{4.5}$	178	31,623	270
10^5	316	100,000	860
$10^{5.5}$	562	316,228	2700
10^6	1000	1,000,000	8600

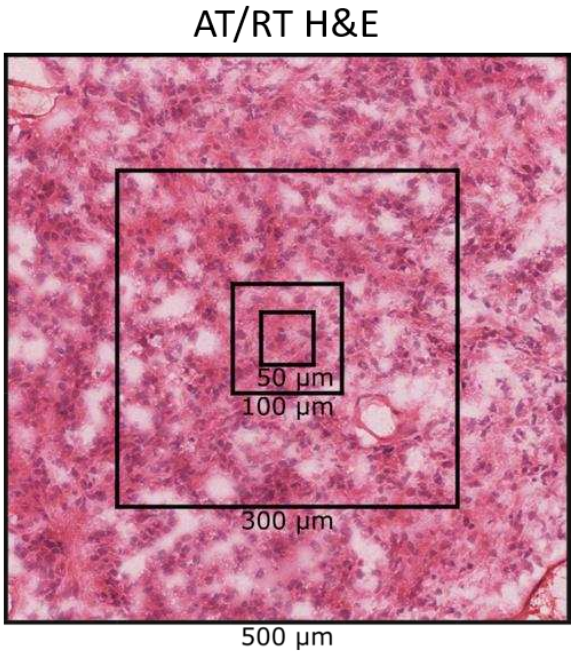

Figure S1 – Tissue area titration across two LC-MS/MS systems
The number of proteins identified from a titration of AT/RT tissue area on two LC-MS/MS systems.

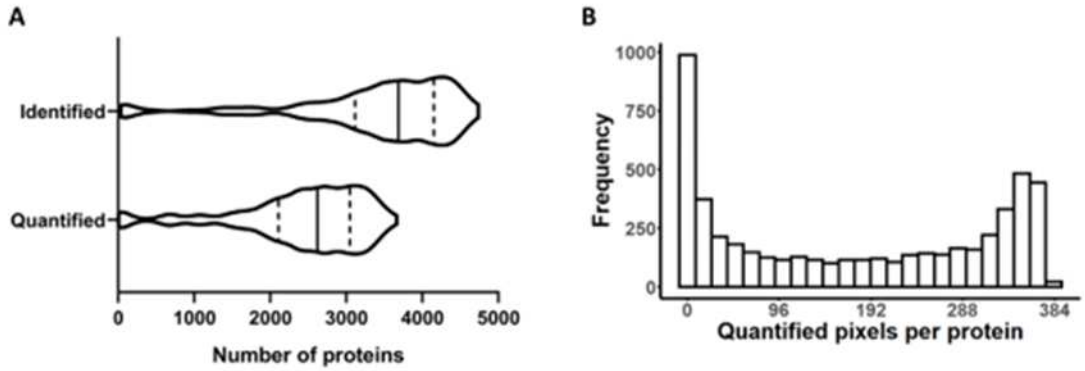

Figure S2 – Distribution of identified and quantified proteins at 833 µm resolution
(A) Violin plots showing distributions of identified and quantified proteins per pixel. Solid vertical lines represent the median value. Dashed vertical lines represent upper and lower quartiles. (B) Histogram of quantified pixels per protein map.

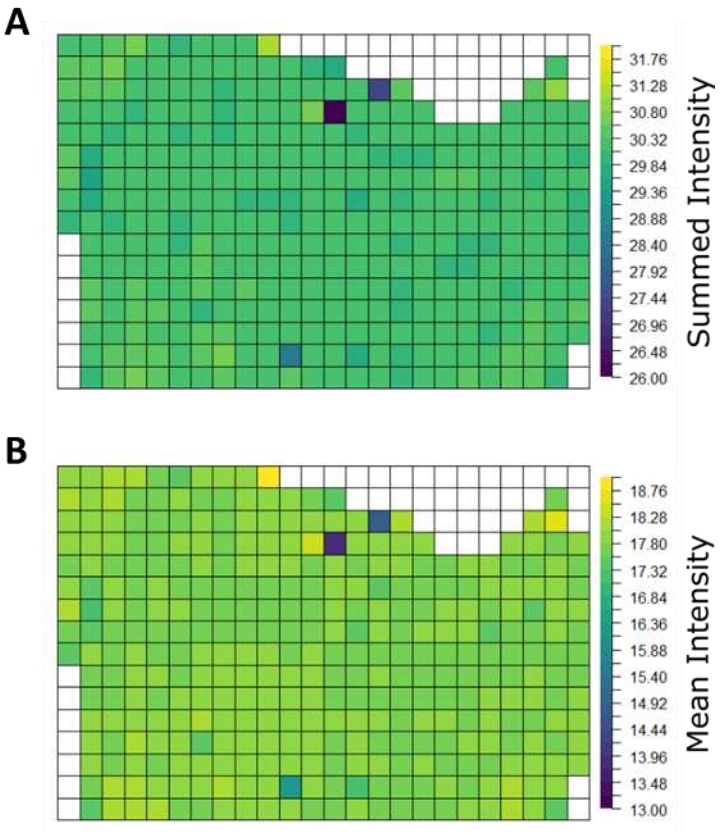

Figure S3 – Aggregate intensity distributions

Maps of the $\log_2$ transformed (A) summed and (B) mean intensities of each pixel. Pixels corresponding to empty or haemorrhage pixels were removed (white).